Journal of Colloid and Interface Science 653 (2024) 1123–1136

Contents lists available at ScienceDirect

Journal of Colloid And Interface Science

journal homepage: www.elsevier.com/locate/jcis

Polarisation and rheology characterisation of monoolein/water liquid crystal dynamical behaviour during high-viscosity injector extrusion

Connie Darmanin [a,1,*], Firoozeh Babayekhorasani [b,c,1], Andrew Formosa [a], Patrick Spicer [c,*], Brian Abbey [a]

[a] La Trobe Institute for Molecular Science, Department of Mathematical and Physical Sciences, School of Computing Engineering and Mathematical Science, La Trobe University, Bundoora, VIC 3086, Australia
[b] Graduate School of Biomedical Engineering, University of New South Wales, Sydney, NSW 2052, Australia
[c] School of Chemical Engineering, University of New South Wales, Sydney, NSW 2052, Australia

GRAPHICAL ABSTRACT

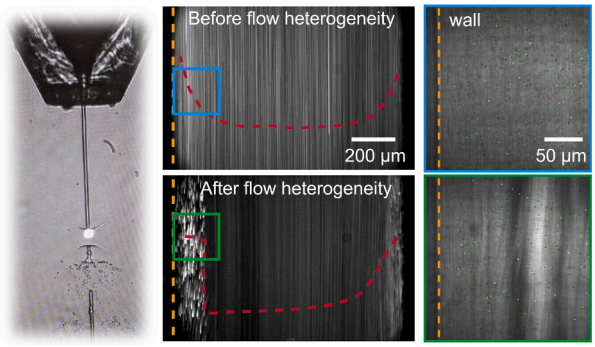

ARTICLE INFO

Keywords:
Lipidic cubic phase
Serial crystallography
High-viscosity
Continuous flow
Lipidico
Mesophase
Phase transition
X-ray scattering
Rheology
Liquid crystals
Monoolein

ABSTRACT

Hypothesis: The use of monoolein/water mixtures in serial crystallography experiments using high-viscosity injectors (HVI) results in significant departures from equilibrium behaviour. This is expected to include changes in phase, viscosity, and associated flow behaviour. It should be possible to detect these changes, in-situ, using a combination of polarisation and rheology characterisation techniques.
Experiments: A systematic study was performed using monoolein, varying the water content to create a range of mixtures. Injection induced phase changes within the HVI flow were established using real-time cross-polarization measurements. Dynamic flow characteristics and viscosity was characterized by particle tracking and rheology.
Findings: HVI injection induces deformation and phase changes within monoolein (MO)/water mixtures which can be detected through variations in the transmitted intensity during in-situ polarisation studies. The heterogeneity of the extruded sample results in a highly viscous cubic phase in the central region of the stream and a

* Corresponding authors at: School of Computing Engineering and Mathematical Science, Department Mathematics and Physical Sciences, La Trobe University, Bundoora, VIC 3086, Australia.
E-mail addresses: c.darmanin@latrobe.edu.au (C. Darmanin), f.babayekhorasani@unsw.edu.au (F. Babayekhorasani), 19954162@students.latrobe.edu.au (A. Formosa), p.spicer@unsw.edu.au (P. Spicer), b.abbey@latrobe.edu.au (B. Abbey).
[1] Equal first authorship.

https://doi.org/10.1016/j.jcis.2023.09.093
Received 4 May 2023; Received in revised form 1 September 2023; Accepted 14 September 2023
Available online 21 September 2023

less viscous lamellar-rich phase at the edges adjacent to the walls. The extent of these variations depends on sample composition and injection conditions. Shear-thinning behaviour and increasing heterogeneity in the vicinity of the capillary walls under dynamic flow conditions. This is the first report observing injection induced dynamical behaviour in MO/water mixtures under realistic flow conditions.

1. Introduction

Monoolein (MO) is well-known for its remarkable aqueous self-assembly properties and over the past few years has emerged as one of the most important lipids impacting many fields including cosmetics, food additives, emulsifiers, drug delivery and protein crystallography [1]. In the context of structural biology MO has played a key role in helping to obtain the structures of many hard-to-crystallise proteins [2–7] and been used extensively as a carrier medium in order to control the delivery and release of drugs [8–17]. The high viscosity and biocompatibility of MO also means that it has also recently been used as a carrier stream for serial crystallography experiments utilising high-viscosity injectors (HVIs) aimed at determining protein structures from small crystals [14,17–21]. High-viscosity injectors are designed to deliver sample, typically small protein crystals, to the X-ray beam in a continuous flow geometry. Monoolein/water is one of the most common media used as a high-viscosity carrier medium due to its ability to provide a suitable environment for both growing and delivering crystals to the beam [14,17] In these HVI experiments large numbers of small crystals encapsulated in a MO/water mixture are continuously extruded from a small capillary tip after which the stream intersects with the X-ray beam and a diffraction pattern is recorded. By continuously replenishing the crystals at the interaction region of the X-rays and the lipid stream a large number of diffraction patterns can be recorded resulting in retrieval of the crystals molecular structure. However, the dynamic flow conditions encountered in the HVI and the effect this may have on the extruded MO/water mixture has not been widely investigated in the literature.

The complex dynamic behaviour of MO and its ability to adopt a variety of mesophases which can be tailored under different conditions, has motivated a significant amount of research into its physical properties and phase behaviour. Through decades of research, we have come to understand that monoolein's phase behaviour depends on a variety of factors including solvent composition, temperature, and pressure. Several strategies have been devised to utilise the response of the MO phase to these factors, enabling effective control over the lipid's behaviour [22–30]. Continuous research into the relevant phase diagrams has also generated a deeper understanding of the lipid behaviour within controlled environments and for a variety of different conditions.

Whilst the structure of lyotropic liquid crystals, formed by self-assembled lipids, such as MO in water have been well studied using X-ray diffraction techniques over the past few decades [22,26,27,29], there has been comparatively little work conducted to characterise the rheology of these samples and thus to understand their viscoelastic properties under continuous flow conditions [31–38]. Jones and McLeish [31] studied the rheology of cubic phases and modelled the slip-plane theory which describes the shear yielding of these samples. They suggested that when the system experiences stress beyond a critical value, slip planes emerge. This leads to a bulk relaxation phenomenon where the sample maintains its network structure while behaving like a liquid. It moves by flowing within a slip layer, rather than through the breaking and reforming of crystalline unit cell bonds due to dislocations [31]. Assuming a pseudolinear response, the authors were able to determine values for the storage and loss moduli as a function of oscillatory shear frequency.

Halász et. al [39] also studied the structural and viscoelastic properties of liquid–crystal systems and observed complex rheological behaviour. They found that the orientation of lamellar liquid crystals subjected to shear forces can change. The orientation of the lamellar in the non-sheared state was found to depend on the domain-domain interactions within the sample, however, when subjected to stress the sample orientation of the lamellar domains is altered and the competition between the domain interactions and the external stress on the system alters the viscosity of the system [39]. They also observed the storage modulus was dependent on the shear frequency as described by the Jones and McLeish [31] slip-plane theory, the value for the loss modulus however did not initially agree with the earlier findings. It was only when a change in orientation of the lamellar domains was considered, a feature described by the Larson and Doi model of liquid crystalline flow [40] and experimental work [41], that values for the loss modulus could be defined correctly.

Mezzenga et. al. [25] also characterised specific rheology signatures for different phases within MO/water systems based on the storage and loss moduli and relaxation times. Using a combination of Small Angle X-ray Scattering (SAXS) and rheology studies they developed a model of the viscoelastic behaviour of a structured fluid. They characterised the lamellar phase as having a stress plateau consistent with slip-plane or sliding flow similar to that suggested above for yielding cubic phases. Whilst previous studies have mostly considered the low-strain rheology of liquid crystalline samples; many applications require much higher levels of deformation. A recent study of large-amplitude oscillatory strains (LAOS) of different MO/water phases found cubic phases yield around 1 % strain and exhibit complex thinning and thickening behaviour at higher strains [42]. Because such bulk rheology measurements assume a homogeneous flow field in the sample, the slip-plane form of yielding exhibited by cubic phases makes the interpretation of such data at high strains more difficult. Even more difficult is the prediction of how cubic phases behave at the very high strain magnitudes which are routinely employed during mixing, pumping, and dispensing of commercial complex fluids. These higher strains occur over length scales much larger than typically used in rheology experiments but are comparable to those used in lipid injectors. In such cases additional information is needed on the flow profile, in an analogous geometry, for accurate description and prediction of the flow of shear-thinning complex fluids with a yield stress [43].

A review of the literature reveals that MO behaviour is complex and a clear understanding of its mechanisms relating to phase change, particularly in the context of external shear, is currently not well-understood. As a structured fluid which does not obey a simple linear relationship between applied stress and flow, this material may be expected to have a viscosity that decreases at higher rates of shear velocity/stress, commonly known as 'shear thinning'. Three factors that need to be considered when characterising these lipids are the internal structure of the sample, the external force exerted on the sample, and the local environment surrounding the sample, all of which will have a major influence on its behaviour. It is not until we understand the interplay of these various factors and how they relate to the properties of MO that further applications for this lipid (and other similar materials) can be fully explored for characterisation studies using HVIs. An important conclusion from previous studies [23,44] is that the structure and rheology of viscoelastic liquid crystals like MO are likely to be altered by flow through an injector. Typical assumptions related to homogeneous flow, such as those often used to model flow in Computational Fluid Dynamics (CFD) simulations, can also be highly inaccurate if flow-induced phase separation and flow heterogeneity are not well understood.

In previous work, [23,44] we investigated the structural changes that occur in MO under continuous flow conditions using X-ray diffraction.

These studies showed that the MO phase varies along the length of the stream and adopts co-existing lamellar and cubic phases (Pn3m and Ia3d) [23,44]. Finite Element Modelling (FEM) studies predicted that a change in dynamic viscosity of MO should occur during the injection process which we hypothesised is likely the dominant cause of phase changes occurring within the viscous sample stream [44]. A follow up study verified the formation of two co-existing phases, cubic and lamellar, in the initially homogeneous lipid sample is a direct result of the sample injection process [23].

Here, we investigate the physical properties of MO/water mixtures under continuous flow conditions using a combination of rheology and in-situ optical cross-polarisation techniques in order to understand its behaviour during high-viscosity injection. In the present case we examine the behaviour of the HVI during the short time after injector initialisation and treat the extrusion of the monoolein/water mixture into air as an open system. This means that the behaviour of the fluid flowing within the HVI should be considered to be 'dynamic' versus 'static' behaviour. Hence, we refer to the monoolein/water characterised in this paper as having dynamic rather than static properties – this is also in line with experimental observations. The use of cross-polarised microscopy, during sample injection, allows us to track the change in phase along the sample stream as it exits the needle. For these measurements a variety of different flow rates were applied which subject the MO/water stream to different shear forces inside the HVI. Rheological studies were carried out to assess corresponding changes in mechanical properties of the sample under similar stress/strain conditions as applied in the HVI. Supporting the bulk behaviour studies, flow visualisation is also used to identify conditions where flow is homogeneous as described by previous simulations [44], but also where flow becomes heterogeneous and the liquid crystal structure likely changes. These studies provide new insights into the viscoelastic origins of dynamic phase changes within MO during HVI and offer new insights into control and optimisation of the mesophase for HVI characterisation studies.

2. Methods

2.1. Sample preparation

Monoolein (1-Oleoylglycerol) obtained from Sigma-Aldrich®, and Milli-Q H_2O (18.2 MΩ.cm) were used to prepare MO/water samples. The samples were prepared as previously outlined in Wells et.al [23]. A standard LCP syringe mixing protocol was used to create different percentages of MO/water mixtures in the gas-tight 100 ml Hamilton glass syringe coupling system [Hamilton syringes, 7656–01, Formulatrix coupler, FMLX Part 209,526 [45,46]. Briefly, the appropriate amount of dried MO was added to one syringe and the appropriate amount of water was added to a second syringe and the samples mixed together using a gas tight 100 μl Hamilton glass syringe coupling system (Hamilton syringes, 108 μm diameter bore size, 7656–01). The following samples of MO/water (w/v) were made up in the syringes: 50 wt% MO, 60 wt% MO, 70 wt% MO, 85 wt% MO. Four syringes were prepared for each sample composition and tested in the injector under different flow rates.

2.2. Injector set up and cross-polarisation camera imaging

A custom setup was developed as part of this project to enable the optical polarisation data to be collected during sample injection. The glass syringes containing the sample were directly loaded into a high viscosity injector, the Lipidico injector [47,48]. This injector was used to generate the lipid stream maintaining a constant flow. The flow rate was adjusted between 0.4 and 3.9 nl/s (40 to 410 μm/s). Initially, a systematic investigation of the injector system was conducted within this range, using increments of 0.4 nl/s. Notably, alterations in the polarization stream manifested exclusively at these particular flow rates, and hence they were selected for further comprehensive investigation. The peak flow rate within the channel serves as a robust demonstration of how flow irregularities contribute to the formation of a slip layer adjacent to the wall, which in turn triggers a rise in the speed of the fluid. To capture the polarisation-mediated transmission of the sample stream, a camera (I-Speed 2 series camera by IX Cameras) station was set up with Lipidico on an optical bench, with the addition of two linear polarisers (Thorlabs) oriented at 90 degrees with respect to one another (i.e., extinction condition). The polarisers were placed either side of the continuous sample stream. One polariser was fixed in place attached to the LED light source while the second polariser was placed between the camera and the sample stream and was able to rotate 90°. All polarisation studies were carried out under standard temperature and pressure (STP) conditions. From this data representative still images were extracted for the figures presented in this paper and the intensity differences along the stream analysed and plotted using ImageJ [49].

2.3. Rheology measurements

Rheological behaviour of the samples was measured using a DHR Rheometer (TA Instruments) and a parallel plate geometry with diameter of 8 mm at a temperature of 26 °C. The gap was adjusted to 200 μm. Rheology was performed at shear rates of 0.1 – 100 s^{-1}. A strain sweep measurement was used to determine the linear viscoelastic regime (LVR) for each sample at a constant frequency of 1, 5, or 10 rad/*sec*. A frequency sweep was performed at a constant strain value within the LVR for frequencies of 0.1 – 100 rad/s to measure the viscoelastic moduli of the MO liquid crystal samples at small strain amplitudes to minimize induced structural effects.

2.4. Flow characterization

Carboxylate polystyrene fluorescent microspheres (Polysciences) with a diameter of 1 μm and 2.5 % solids (w/v) were diluted 500x in the mixture of 60 % monoolein/water. A 1 ml glass syringe (Hamilton Co, Reno, Nevada) filled with the sample was connected to a square capillary with an inner diameter of 0.9 mm and wall thickness of 0.18 mm (VitroCom) using Tygon tubing with an inner diameter of 1.6 mm. A syringe pump (WPI 947–371-1003) working at constant displacement with nominal flow rates of 100, 500, and 1000 μl/h was used to feed the square capillary. The flow in the capillary was imaged using an upright Leica DM2500M microscope with a 20x air objective (NA = 0.4) at a frame rate of 20 fps (Moticam 10MP, Motic) and an upright confocal Zeiss LSM 900 microscope with a 63x immersion oil objective (NA = 1.4) and framerate of 2.17 fps. Particles were tracked over time using a single particle tracking algorithm in MATLAB [50]. Velocities of the particles were calculated based on the measured particle trajectories over time.

3. Results

3.1. Polarisation results

As a control, different phases of MO were tested in the injector to measure the changes in polarisation-mediated transmission. Pure cubic phases are not expected to cause any rotation of the incident polarisation vector and thus have no birefringence (no transmission). Therefore, any observation of birefringence in the sample implies a structural phase change has occurred. Using the phase diagram [26,27], samples were prepared with varying water content to form different phases which exist for MO when mixed at room temperature. Based on the phase diagram, the samples are expected to have the following initial phase prior to injection: 50 % MO sample will result in a cubic phase containing excess water; 60 % MO will result in a *Pm3m* cubic phase; 70 % MO will result in an *Ia3d* cubic phase; 85 % MO will result in a lamellar phase. When the linear polarizers are at the extinction condition, a measurable transmission occurs if the sample phase induces a rotation of the

polarization vector. This indicates the presence of an optically anisotropic phase in the sample (Fig. 1). The observed change in birefringence suggests the presence of a lamellar phase. The decrease in the density and viscosity of the mixture during continuous flow of the sample supports this interpretation since the phase diagram suggests that hexagonal phases only occur at higher temperatures then the ones used in this study. For each measurement the sample flow reached a stable steady-state condition before an analysis of the sample birefringence was performed.

Four sample syringes were tested for all sample compositions. For the 50 % MO sample, in each case birefringence was observed. However, there was some variability in terms of the flow rates required to induce sample birefringence. Two syringes exhibited birefringence at higher flow rate (1.9 nl/s and 3.9 nl/s) and the other two syringes only at the lower flow rate (1.2 nl/s). Fig. 1 presents example data collected from the 50 % MO, 60 % MO, and 70 % MO samples at three different flow rates. Analysis of the light intensity within the stream during sample injection suggests that the sample stream is more birefringent (higher intensity) closer to the needle tip at a flow rate of 1.9 nl/s, whilst at 3.9 nl/s the highest intensity is detected further downstream at a greater distance away from the tip.

For the 60 % MO sample (Fig. 1b and 2), at low flow rates of 1.2 nl/s birefringence of the sample was detected and persistent along the majority of the length of the lipid stream for all of the syringes tested with varying intensity. Fig. 1 compares the birefringence of the sample at higher flow rates. With an increase in flow rate to 1.2 nl/s the 60 % MO sample showed no signs of birefringence close to the needle tip (<100 μm), however, further away from the needle tip (>300 μm distance) the stream started to exhibit weak birefringence (Fig. 2). An enlarged view of the sample stream flowing at 1.2 nl/s is shown in Fig. 2b along with a zoomed in view of the downstream portion of the sample stream (Fig. 2c). When the flow rate was further increased to 1.9 nl/s the intensity of the birefringence within the sample stream also increased starting at 200 μm downstream of the needle point, this is clearly seen in the intensity profiles (e.g., Fig. 1b). At the fastest flow rate, 3.9 nl/s, the sample behaviour changed, and no signs of birefringence were detected in the sample stream.

As the MO content of the sample was further increased to 70 % MO, a larger signal of birefringence was detected at all three sample flow rates (Fig. 1c). The birefringence intensity also increased significantly

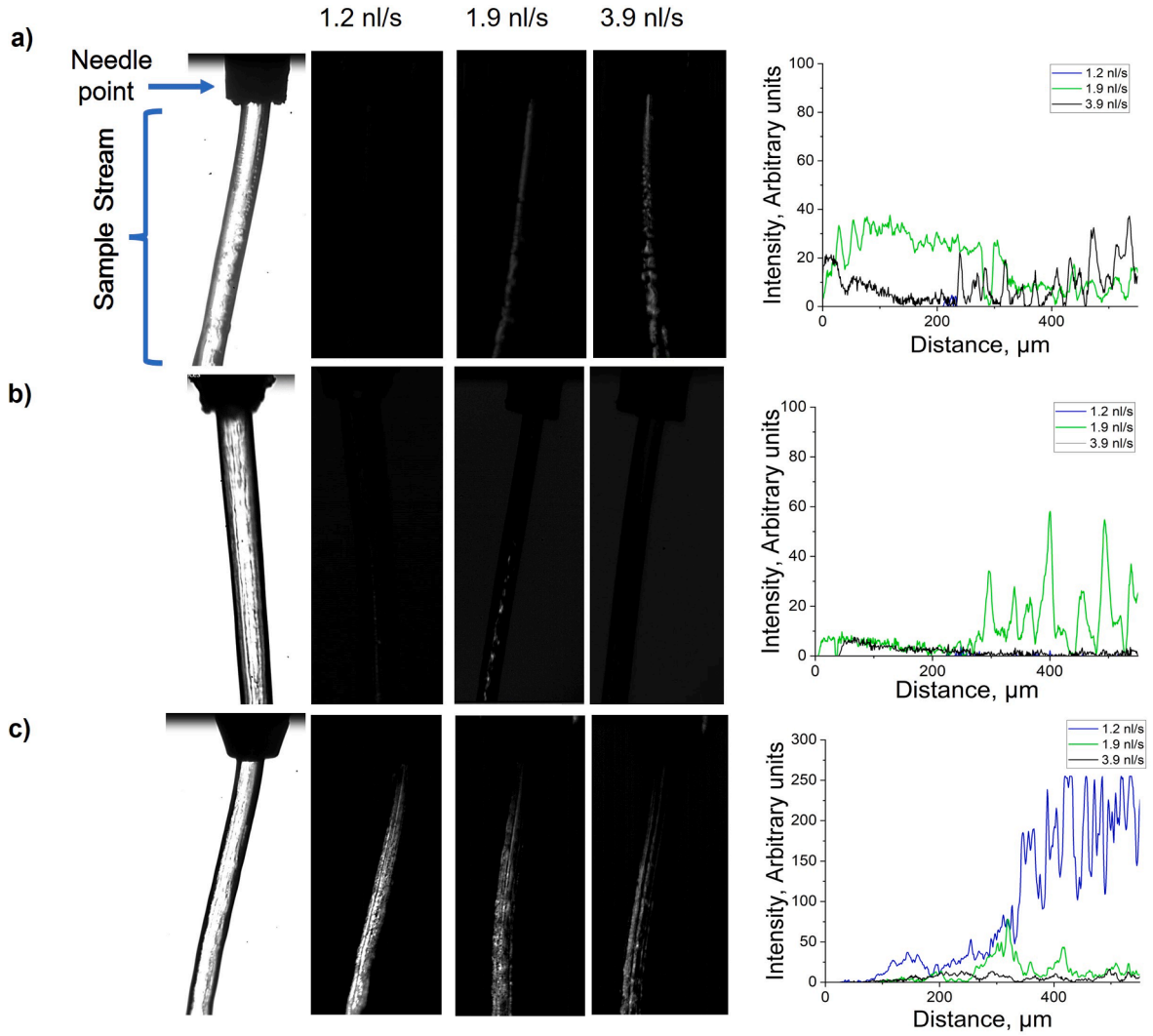

Fig. 1. Optical microscopy images showing the birefringence present in in the MO/water sample **a)** 50% MO, **b)** 60% MO and **c)** 70% MO during continuous streaming from the injector. The left-hand column shows the conventional brightfield microscopy images for comparison. The three images to the right of this show light transmission through the sample using two linear polarisers oriented at the extinction condition ('cross-polarisation'). The values at the top of each of the three cross-polarisation images are the flow rate. Plots to the right-hand side of the images are the light transmission intensity obtained by averaging the pixel values in the direction perpendicular to the direction of flow to obtain the average light transmission intensity along the stream. All intensities are normalised to the same value and so may be compared directly.

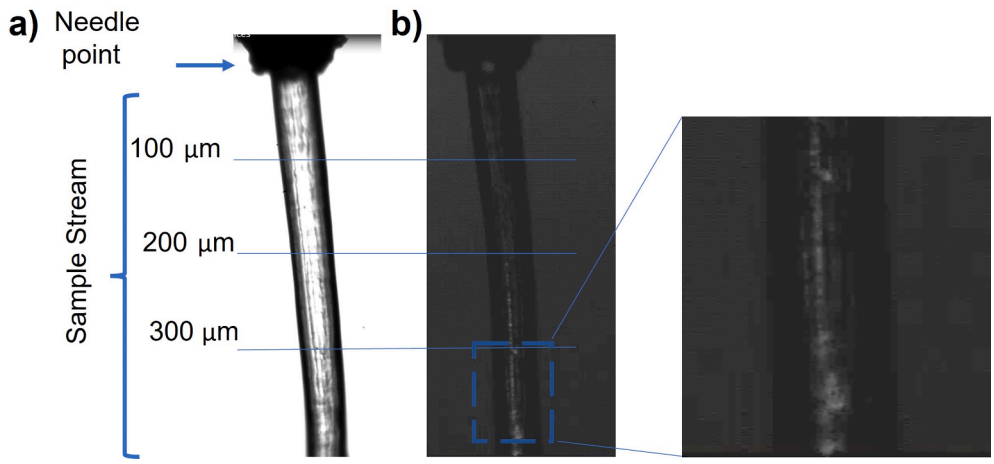

Fig. 2. Optical microscopy images providing a closer view of the birefringence present in the 60 % MO sample during continuous streaming at 1.2 nl/s from the injector. **a)** Brightfield image **b)** cross-polarisation image and an enlarged view of the region far away (>300 µm) from the needle tip. Different distances from the needle tip (inner diameter = 108 µm) are indicated by the horizontal dashed lines.

compared to the previous samples, with the 1.2 nl/s flow rate exhibiting the greatest birefringence along most of the sample stream. The birefringence was then observed to decrease as the flow rate was increased within the sample.

The above results are consistent with the expectation that a lamellar liquid crystal structure can form as a metastable structure during flow. Once formed, the lamellar phase can adopt different morphologies and alignments depending on flow intensity and orientation [41]. While most flow seems to lead to some form of lamellar phase, not all forms are optically birefringent and this could explain, for example, the relaxation behaviour seen upon increased flow.

Above 70 % a stable flow could not be obtained using the HVI injector – this was characterised by bubbling at the needle tip, rather than the stable formation of a continuous stream (Supplementary Fig. S1). Hence, higher fractions of MO were not extensively analysed for the real-time birefringence study but were analysed for the rheology study.

A second set of injector tests was performed to evaluate the sample's response to rapid changes in flow rates, i.e., non-steady state flow conditions. The HVI (Lipidico) injector allows for spontaneous changes in flow rate, and our results showed that a sudden jump from a high flow rate 3.9 nl/s to a low flow rate of 1.9 nl/s could reproducibly introduce a change in birefringence of the stream. Fig. 3 illustrates this effect for the 60 % MO, where an increase in birefringence was detected within 0.4 s of the initial flow rate change, and the intensity increased for an additional 0.13 s before decreasing and returning to a non-polarized state again (after 0.56 s, Supplementary Video 1 shows the live streaming of the sample). This may indicate that following a sudden change in shear force experienced by the sample there is a relaxation time after which the lipid returns to its original state. This same effect was also observed in the 70 % MO sample. The formation of a birefringent, presumably lamellar, phase during slower flow is likely the result of the high-deformation regions of the liquid crystal structure slowly relaxing. Such behaviour is qualitatively consistent with previously published results for liquid crystalline structures observed during strain reversal experiments, where collective motion of self-assembled regions of the texture were responsible [40].

3.2. Rheology results

The rheological behaviour of the MO/water mixture was studied at different concentrations of MO at a temperature of T = 26 °C. The results showed that the shear viscosity significantly decreases as the shear rate increases for mixtures with 60 % and 70 % MO, indicating a strong shear-thinning profile (Fig. 4a) for the presumed cubic phases. The shear viscosity reduces by about 3 orders of magnitude over the range of shear rate between 0.1——100 rad/s. The shear viscosity scales with shear rate as $\eta \approx \gamma^{-0.94}$ for 60 % MO and $\eta \approx \gamma^{-0.87}$ for 70 % MO. For the highest MO

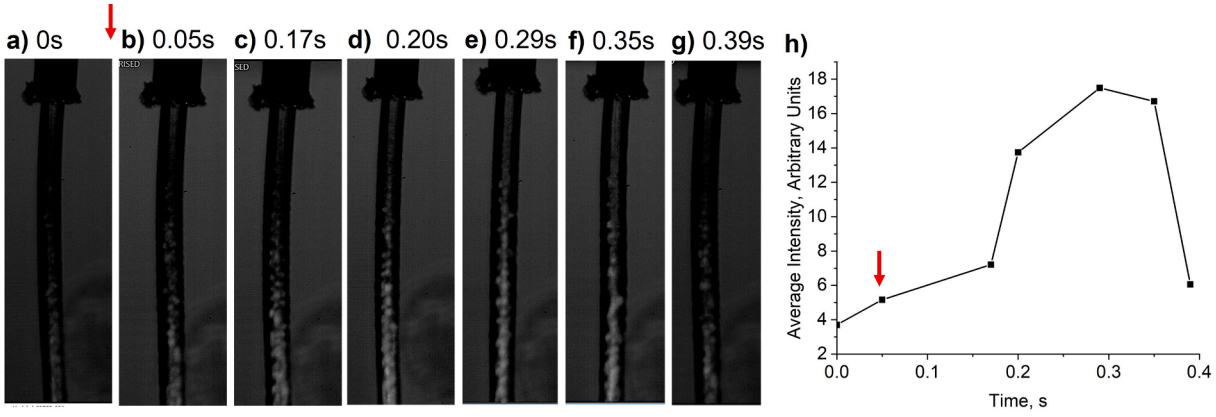

Fig. 3. Time dependence of birefringence following instantaneous flow rate change for the 60 % MO sample. a) Example images from supplementary Video S1 showing variations in birefringence. The time points following the initial change in flow rate which occurred at t = 0.05 s (indicated by the vertical arrow) are shown above the images. b) Plot of the average transmission intensity measured along the sample stream shown in a) as a function of time. Note, a) The images have been contrast-enhanced to render the transmission through the polarized stream visible. The raw average transmission data (without any post-processing) is plotted in b).

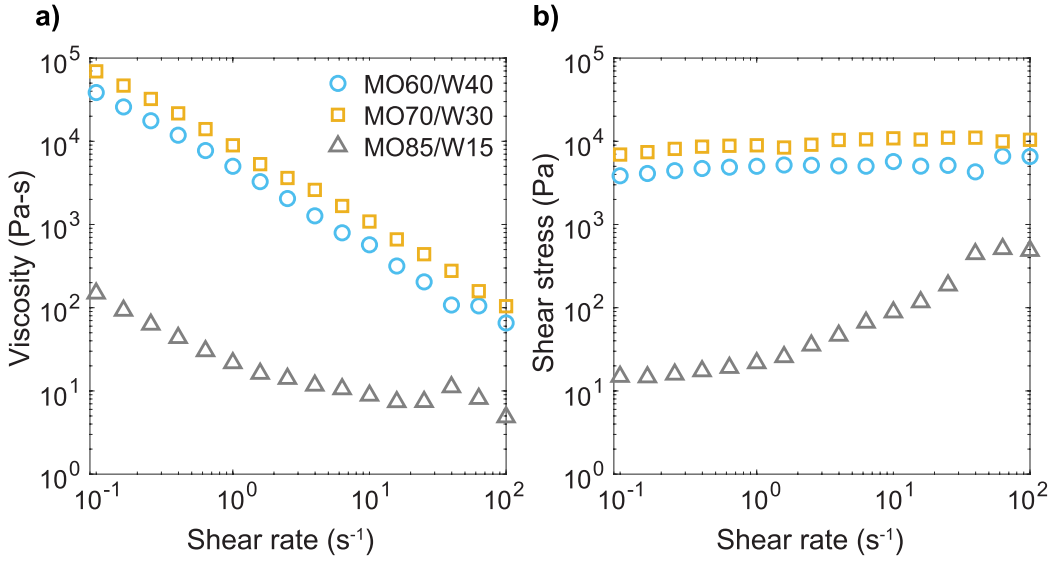

Fig. 4. Shear rheology of MO/water mixture depends on the liquid crystalline phase. **a)** Shear viscosity as a function of shear rate for 60% MO (circles), 70% MO (squares), and 85% MO (triangles) at 26°C. **b)** Shear stress as a function of shear rate for 60% MO (circles), 70% MO (squares), and 85% MO (triangles) at 26°C.

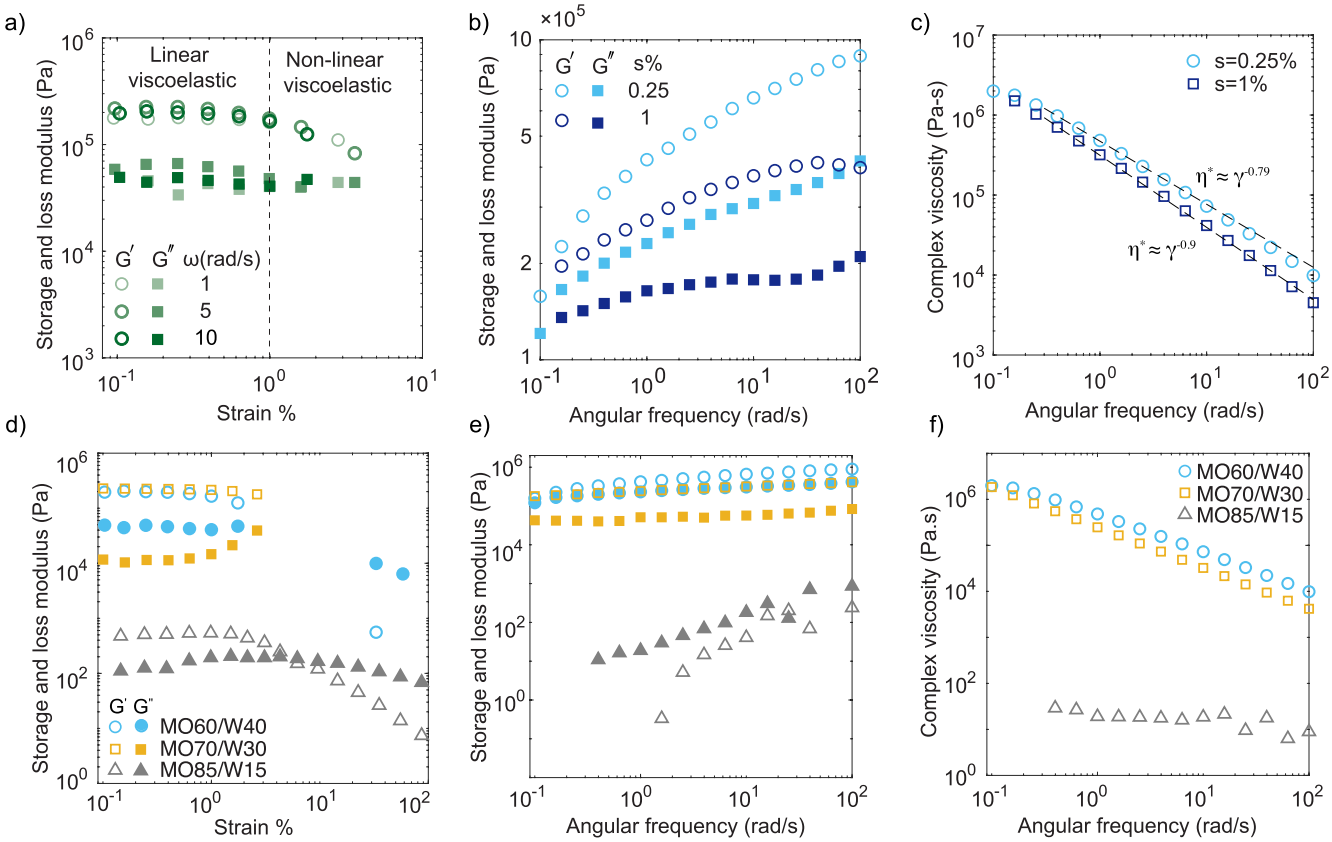

Fig. 5. Angular frequency plots. **a)** Strain sweep measurements of 60 % MO sample at frequencies of 1 (light green), 5 (green) and 10 rad/s (dark green) at 26°C. The change in the elastic (open circles) and viscous modulus (closed squares) as a function of strain is displayed. **b)** Elastic (open circles) and viscous modulus (closed squares) are measured for a frequency range of 0.1 – 100 rad/s at strain of 0.25 % (light blue) and 1 % (dark blue). **c)** Complex viscosity as a function of frequency, range = 0.1 – 100 rad/s at 0.25 % (light blue) and 1 % (dark blue) strain. **d)** Strain sweep measurements of MO/water with 60 % MO (blue), 70 % MO (yellow) and 85 % MO (grey) shown at constant frequency of 10 rad/s. **e)** Elastic (open symbols) and viscous modulus (closed symbols) are measured for the frequency range of 0.1 – 100 rad/s within the linear viscoelastic region for MO/water with different MO concentrations of 60 % MO (blue), 70 % MO (yellow), 85 % MO (grey). **f)** Complex viscosity as a function of frequency for MO/water with 60 % MO (blue), 70 % MO (yellow), 85 % MO (grey). (For interpretation of the references to colour in this figure legend, the reader is referred to the web version of this article.)

concentration of 85 %, the low shear viscosity is three orders of magnitude smaller than the high shear viscosity of the cubic phase, as a result of the system's lamellar phase structure. For 85 % MO, the shear viscosity scales with shear rate as $\eta \approx \gamma^{-0.24}$, indicating a weaker shear-thinning behaviour compared to the other concentrations with a cubic phase structure. The power-law exponent represents the degree of thinning exhibited by non-Newtonian fluids, where the exponent is −1 for plastic deformation [25] and zero for Newtonian fluids. The estimated exponent is close to −1 for the cubic phase mixtures (60 and 70 % of MO) indicating a near-ideal plastic deformation of the mixtures, with perhaps some residual viscous resistance [25]. Such behaviour is consistent with our expectations based on the slip-plane yielding theory [31] and past results for ternary cubic phase systems [32], but the implications of this behaviour are significant for strong flows such as those produced in the HVI.

For the cubic phase mixtures, the shear stress remains roughly constant for a range of different shear rates (Fig. 4b). This is consistent with the estimated power-law exponent for viscosity vs shear rate as $\eta \approx \gamma^{n-1}$ so $\tau \approx \gamma^{n}$. This means that as the shear rate increases, the cubic phase systems can be made to flow at higher rates without additional stress being required, presumably because the system moves on a transient liquid layer wherever it yielded earlier.

In Fig. 4b, the fluctuation observed (between 10 and 100 1/s range) in the shear stress between the different samples could be related to flow heterogeneity, specifically at higher shear rates. For the lamellar phase mixture (85 % MO), the shear stress decreases with decreasing shear rate and plateaus at low shear rate (Fig. 4b). The low-shear stress values are much higher for cubic phase mixtures (3.8×10^3 and 6.9×10^3 Pa for 60 and 70 % MO respectively) compared to the lamellar phase mixture (14.8 Pa) indicating that the minimum force, or yield stress, required for the cubic system to flow is much higher than for the lamellar phase system.

The frequency-dependent rheological behaviour of the 60 % MO sample was measured to understand the viscoelastic properties and compare with past work (Fig. 5a). The strain sweep of the mixture was performed at constant angular frequencies of ω = 1,5,10 rad/s for strains of 0.1–10 %. The MO/water mixture exhibits roughly linear viscoelastic behaviour for strains smaller than 1 %, consistent with Jones and McLeish [31], as well as Mistry et.al. [42] findings. Within the linear viscoelastic regime, the elastic and viscous modulus are roughly constant for increasing strain. The storage and loss modulus of the mixture were measured at a strain of 0.25 % within the linear viscoelastic regime and at a strain of 1 % where deviation from linearity begins (Fig. 5b). At a strain of 0.25 %, the dependence of the storage and loss modulus on frequency exhibits an elastic dominant behaviour for small deformations (G' > G'') in the cubic phase mixtures over the frequency range of ω = 0.1–100 rad/s. Storage and loss modulus both decrease as frequency decreases. A cross-over point between the storage and loss modulus was not observed. The longest relaxation time of the mixture is then probably higher than the total measurement time, indicating a soft glassy fluid. At a strain of 1 %, the elastic and viscous modulus are smaller compared to the values at a strain of 0.25 %, indicating flow heterogeneity contributes to the reduction in the moduli at 1 % strain. To ensure pre-shearing was not present in our samples prior to testing, flow sweep experiments were performed and were found to be consistent with previous studies [51,52]. Initial experiments at low shear rates (0.1 1/s) ensured that the sample was homogenous prior to the frequency sweep tests.

The complex viscosity estimated as $\eta^* = \frac{\sqrt{G'^2+G''^2}}{\omega}$ reduces as angular frequency increases. The complex viscosity scales with frequency as $\eta^* \approx \omega^{-0.79}$ for a strain of 0.25 % and scales with frequency as $\eta^* \approx \omega^{-0.9}$ for a strain of 1 %. The power-law exponent of the complex viscosity at higher values of strain is closer to the power-law exponent estimated from the shear rheology, which indicates some similar yielding phenomenon quickly reduces the viscosity with increasing shear rate, even at such a relative low value of strain. At a lower strain of 0.25 %, the power-law exponent is smaller, as yielding is not expected during oscillatory measurement within the linear viscoelastic regime (Fig. 5c). The oscillation stress increases as the angular frequency increases (Fig. 5c) consistent with the complex viscosity. The dependence of the oscillation stress on the frequency is less for a strain of 1 % compared to a strain of 0.25 %.

The frequency-dependent rheology of MO/water mixtures at varying concentrations reveals how the phase of the mixture influences both the elastic and viscous responses of the system to changes in angular frequency (Fig. 5d – f). Frequency sweeps of the cubic phase samples (60 % and 70 % MO), when evaluated within the linear viscoelastic domain (Fig. 5e), predominantly display an elasticity-driven behavior. In contrast, the lamellar phase sample (85 % MO) leans towards being viscous dominant, as illustrated in Fig. 5e. The complex viscosity of the lamellar sample is notably lower compared to that of the cubic phase samples, as demonstrated in Fig. 5f. This difference underscores the influence of the intrinsic molecular rearrangements and interactions that define the rheological behavior of each phase. Notably, the cubic phase samples, even with their variations in concentration (60 % and 70 % MO), exhibit similar rheological traits. This consistency suggests the significant influence the fluid phase has in determining the rheological attributes of the cubic phase mixture.

To help connect the rheology results to the continuous flow injector experiments, flow of 60 % MO in a square capillary was also studied to quantify the local response of the viscoelastic cubic phase at different flow rates. Due to the inherent curvature of a cylindrical capillary's circular cross-section, achieving clear microscopy imaging can be challenging. The curved surface may introduce distortions and reflections, compromising the image's clarity and accuracy. Consequently, microscopy imaging was not conducted on capillaries with a circular cross-section. Because the flow profile of fluids is well-understood in different cross-section channels [53], we are able to calculate relevant flow parameters like shear rate and velocity expected for any common geometry channel like these. Fig. 6 shows the trajectories of fluorescent polystyrene spheres embedded in the cubic phase as they move under volumetric controlled flow. The trajectories are coloured by the magnitude of their velocity (Fig. 6 b, c, and d), with red denoting the fastest movement and blue the slowest. The instantaneous trajectories are summarized by plots of the velocity profile (Fig. 6 e, f, and g) that illustrate the relatively uniform flow in the centre of the capillary, also called plug flow, consistent with the behaviour of non-Newtonian fluids [43]. A more parabolic velocity profile, typically associated with Newtonian flow, is seen above 100 μm away from the capillary wall. Depending on the flow rate, the velocity of the internal stream varies significantly, where at high flow (1000 μl/h) it can reach up to 80 μm/s and low flow (100 μl/h) it reduces 10-fold to 8 μm/s. The same is true for the sample speed at the capillary walls. The data suggests that as we increase the flow rate of the sample a larger variation in velocity from the wall to the centre of the stream exists [54,55]. The region where the majority of the flow or sample deformation occurs is similar, though smaller in size, for each flow rate. This indicates that most of the sample is not being deformed at all during flow except within the region next to the wall of the capillary, where shear rates are high and structural transformations are expected as a result of the higher stresses there. The shear rates in that region, however, do change with flow rate, as we would expect for a more generalised description. This suggests that within the central region the stream maintains its cubic phase integrity under constant flow. Whereas the sample closest to the stream walls undergoes a phase change to lamellar due to the shear stress induced by the continuous flow. Although flow heterogeneity may occur, lamellarity in the middle part of the capillary was not restored.

The data in Fig. 6 show well-developed flow consistent with continuum models of power-law fluids [44], but more complex behaviour is observed at longer times, t > 50 s, and at higher flow rates that we document below given the likelihood of their occurrence in injector experiments. Fig. 7 shows similar data to Fig. 6 but specifically

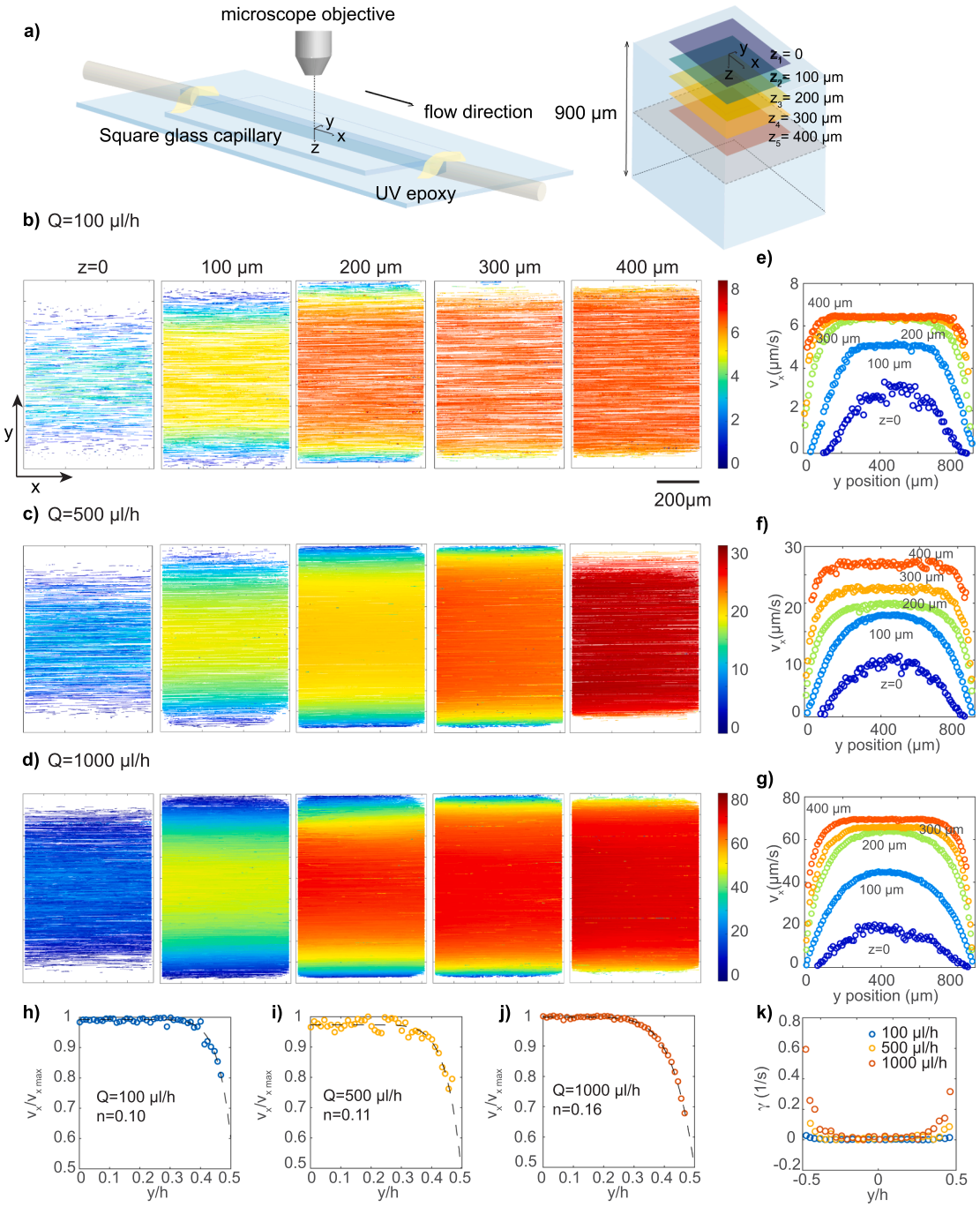

Fig. 6. Flow visualization and profiles for a cubic phase in a square capillary. Schematic diagram of the flow device **a)** and the imaged planes at different z distances from the top surface of the capillary are designated in the right-hand side image. Trajectories of 1 µm particles at each different z plane (0 µm, 100 µm, 200 µm, 300 µm and 500 µm from the bottom of channel, as indicated at the top of the images) were imaged for t = 50 s. The particle velocity along the channel at an inlet flowrate of **b)**100 µl/h (27.8 nl/s), **c)** 500 µl/h (139 nl/s) and **d)** 1000 µl/h (278 nl/s) is represented by colour based on the bar code. Longitudinal velocity along the transverse direction of the flow at different heights of the fluid in channel at the flowrates of **e)** 100 µl/h, **f)** 500 µl/h and **g)** 1000 µl/h are also shown. Normalized velocity profiles (to the maximum velocity) at z 400 µm plotted as a function of normalized distance from the channel centre at the flowrates of **h)** 100 µl/h, **i)** 500 µl/h and **j)** 1000 µl/h. The dash lines represent the fitting of the velocity profile to $\frac{v_x}{v_{xmax}} = 1 - \left(\frac{2y}{h}\right)^{\frac{n+1}{n}}$. **k)** Shear rate of the fluid at z 400 µm as a function of normalized distance from the channel wall. Samples are imaged at a frame rate of 20 fps for 1000 frames.

highlights the occurrence of flow heterogeneity and its inconsistency (Fig. 7a and b). The flow layer near the wall sometimes halted at high flow rates approximately 90 s after the experiment commenced, due to fluid heterogeneities, meaning regions sometimes form stagnation zones where flow stops or recirculation of the flow is low or zero, as observed in Fig. 7. This is confirmed by plotting windows of the data over a time interval using superimposed frames, to indicate trajectories of the fluorescent tracers as streaks whose lengths indicate their velocity. Fig. 7a shows a well-developed plug flow over time at a fixed z-position of 300 µm in the capillary, which is a considerable distance from the surface, consistent with experiment in Fig. 6. Fig. 7b, however, shows a second experiment of the same sample captured approximately 3 min after 7a within the same time intervals with a markedly different flow profile. For example, in Fig. 7b, between 10 and 20 s the upper part of

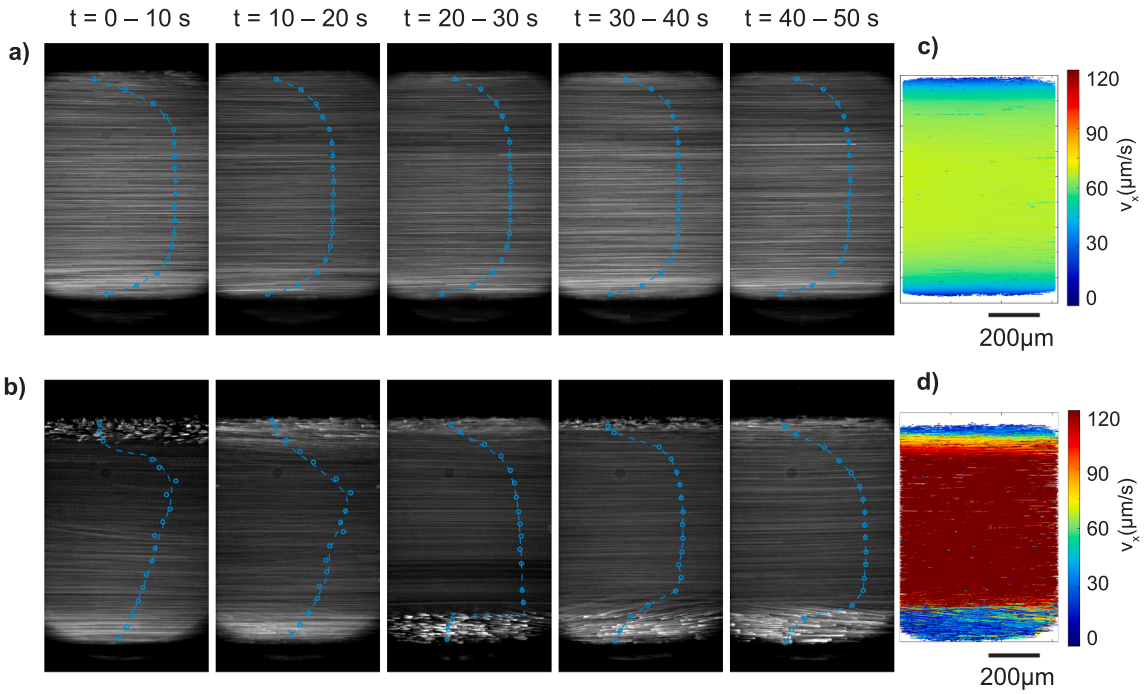

Fig. 7. Effect of flow instability on the velocity profile for 60 % MO sample. Snapshots of the standard deviation of consecutive 200 frames (10 s) of the particle movement along the channel at z = 300 μm at a flow rate of 1000 μl/h, before **a)** and after **b),** flow heterogeneities for various time points (t) denoted at the top of the image. Overlaid graphs (blue circles) show the velocity profile in the longitudinal direction at each time window. Also shown at the trajectories of particle movement along the channel at z = 300 μm, coloured by the longitudinal velocity before **c)** and after **d)** flow heterogeneities. Samples are imaged at a frame rate of 20 fps for 1000 frames. (For interpretation of the references to colour in this figure legend, the reader is referred to the web version of this article.)

the image shows a thin region of very little flow that gradually develops into more plug-like flow in Fig. 7b 20–40 s interval. However, even as the upper region flow becomes more conventional, the lower part of Fig. 7b during the 0–50 s interval, shows a transition between rapidly flowing regions that then decelerate to a much lower velocity in a short time. In the middle of the channel a relatively sharp transition in velocity is visible in Fig. 7b between 0 and 20 s but this discontinuity then smooths out after 20 s duration. The heterogeneous flow is likely a consequence of slip-plane yielding that becomes unstable in the channel. We expect heterogeneous flow to be more of an issue at larger length scales like the capillaries used here as well as the HVIs. Because bulk rheology studies tend to be carried out at much smaller length scales, the effect may not influence their results as much. Because we have not performed these tests in a rheometer, we cannot say for certain that shear banding is occurring, at least not in a reproducible manner. We would, however, like to speculate that these heterogeneities occur in injector flows and provide a preliminary insight into the structures of the flows during heterogeneity formation.

Zoomed-in views of the flow using confocal imaging show captured planes at z = 0, 50, and 100 μm from the capillary surface at a constant flow rate of 100 μl/h (27.8 nl/s, Fig. 8a and b) and at different flow rates of 100 – 1000 μl/h and at z = 50 μm (Fig. 8c and d). Focusing on this region allows tracking of tracers in the region nearest the wall where the majority of flow occurs. At the lowest flow rate, 100 μl/h, particle velocity increases with the distance from the wall (Fig. 8a and b). No flow heterogeneities are observed over the course of the experiment at 100 μl/h (27.8 nl/s).

As the inlet flow rate increases from 100 (27.8 nl/s) to 500 (139 nl/s) and to 1000 μl/h (278 nl/s) at z = 50 μm, the longitudinal velocity of the particles increases, indicated by the change in the colour of the streamlines in Fig. 8c from dark blue to dark red. More interestingly, a time-dependent flow instability appears at the highest flowrate (1000 μl/hr) at z = 50 μm from the capillary surface, Fig. 8e – i. Before formation of the flow instability, particles consistently move faster as they flow farther from the wall, at times smaller than 98 s in the Fig. 8i. Partially polarised images of the background, Fig. 8e do not show any change in the structure over time before the instability and the particles flow normally as indicated by the sum of the consecutive 25 frames (Fig. 8f).

As flow instability occurs, the particles at z = 50 μm immediately become stationary at $t \approx 97$ s, while fluid continues to move at z ≫ 50 μm. The partially polarised images of the structures that form in the flow region indicate some birefringence, indicating a transition from cubic to possibly lamellar structure (Fig. 8g). Such immediate change in the velocity of the fluid at different planes coincides with the temporal and spatial appearance of birefringence during the flow instability. The higher magnification provides a higher resolution view in both time and distance of the onset of the flow instabilities and their characteristic sizes, respectively. The change is relatively rapid, occurring within a span of 100 s, but also quite sharp in its boundary with the difference between the two flowing volumes only a matter of a few microns. Fig. 8h shows the onset of particle flow heterogeneities particularly in the region closest to the wall. Although preliminary, the results are supportive of the explanation for the earlier injector experiments and the birefringence observed there at much larger length scales. While these results are preliminary, they provide sufficient evidence of flow heterogeneity and some shear-banding phenomena in cubic phases to warrant more focused study. As shear banding is well-known to occur in lamellar phases[56], and has recently been described well by a thixotropic constitutive model [57], we are motivated to study this behaviour further in cubic phases to enable similar developments.

4. Discussion

Our study expands upon the existing literature by characterising MO/water behavior within an HVI. Table 1 presents a concise summary of the key findings related to MO/water behaviour that are pertinent to this paper. These findings have been explored using a range of

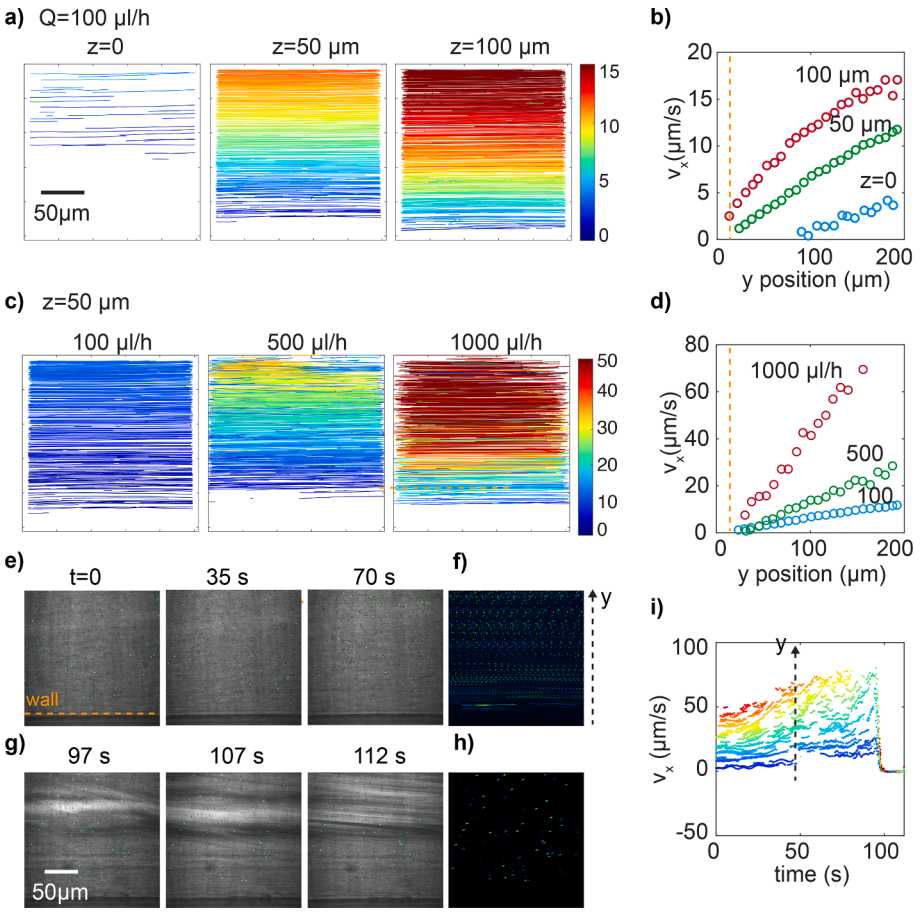

Fig. 8. Confocal imaging of a zoomed-in view of the 60 % MO flow close to the wall. **a)** shows the trajectories of the particle movement along the channel for an inlet flowrate (Q) of 100 µl/h at the bottom of the channel (z = 0) and to additional z distances 50 µm and 100 µm and **b)** shows the longitudinal velocity as a function of distance from the wall at these different z locations. **c)** Trajectories of particle movement along the channel for z = 50 µm at different inlet flow rates of 100 µl/h, 500 µl/h and 1000 µl/h and **d)** shows the corresponding longitudinal velocity as a function of distance from the wall at the different inlet flowrates. The velocity (µm/s) of the particles is indicated by the colour bar on the plots. **e)** Partially polarised imaging snapshots of the particles at different time points 0 s, 35 s and 70 s and **f)** shows the sum of the consecutive 25 frames which exhibit uniform movements of the particles at a flow rate of 1000 µl/h and z = 50 µm, before appearance of the flow heterogeneities. **g)** shows snapshots of the particles at time points of 97 s, 107 s, 112 s and **h)** shows the sum of consecutive 25 frames, showing the onset and continuation of flow heterogeneities in the upper part of the image, while particles close to the wall become stagnant. **i)** Particle instantaneous velocity over time at different y locations, before and after flow instability onset indicated by the dashed arrow.

techniques and in diverse sample environmental conditions. MO is a versatile lipid known for its self-assembly properties and ability to produce different mesophases in water. For example, the highly viscous nature of the cubic phase currently makes it challenging to inject through a needle tip, necessitating the use of additives to induce a lamellar phase mixture for pharmaceutical injection applications [58]. However, if the amount of shear force required to change its phase mixture and thus its viscosity is known, this could avoid the need for additives, which can sometimes have unwanted side effects. Previously Berntsen et.al [44] observed phase changes in MO under continuous flow conditions using X-ray diffraction. The current work points to the fact that shear thinning induced by the injection process could explain the formation of the cubic/lamellar phase mixture previously detected using X-ray diffraction [36]. The addition of polarization light microscopy and rheology provides a new window into the physical properties associated with this phase change under laboratory conditions allowing us to explore a range of sample mixtures and flow rates.

The viscosity of MO/water mixtures slightly decrease when going from 60 % to 70 %, and then significantly decreased at 85 % MO sample. This is consistent with the MO/water phase diagrams [26,27], where the 60 and 70 % MO samples remain in their cubic phase and the 85 % MO shifts to a lamellar phase. This change in viscosity is supported by injector birefringence data, where the cubic phase samples streamed well (Fig. 1), while the lamellar phase (85 % MO) sample did not stream well due to its low viscosity (Fig. S1). This observation is in line with the composition of the sample and the established phase diagrams for MO/water[26,27].

Closer examination of the shear stress in relation to the shear rate (Fig. 4b) provides a deeper understanding of the MO behaviour in the HVI. It revealed possible fluctuations within the 10 and 100 s^{-1} range in the shear stress between different samples. These fluctuations may be caused by flow heterogeneity in the sample at higher shear rates, also known as a “slip” region, which generally indicates a local change in viscosity of the sample is occurring at this point because of a possible phase change that causes shear-thinning. This shear stress range is equivalent to the calculated maximum shear rates for the flow rates tested in the injector system (Table S1), where birefringence was detected within the stream (Fig. 1). This effect corresponded to the 30 to 60 s^{-1} shear rate range in the rheology plots and is also consistent with the co-existence of a lamellar phase and a cubic phase confirmed by X-ray studies[23,44].

To investigate the possible origin of these phase changes detected in both the birefringence data and previous X-ray diffraction studies [23,44] we considered the shear-thinning characteristics of the sample. The shear thinning characteristics of MO/water liquid crystals, a non-Newtonian fluid [25], is a recoverable structural change. Both our

Table 1
A comparative analysis of literature findings and our discoveries through using different Techniques. This table compares the findings from various literature sources with our own experimental results for Monoolein/Water samples. The table focuses on the characterization techniques employed in the studies, highlighting key relevant findings relevant to this study.

Technique	References	Type of Experiment	Key Relevant Finding
X-ray Scattering	[9,106,73,41,46]	Pressure jump studies on MO Temperature-phase composition experiment Continuous flow injector experiment	Visualized the formation, growth, and structure of monoolein liquid crystalline phase Identified co-existing phases and phase transitions in relation to pressure changes. Examined the effect of continuous flow on the stability and alignment of lipidic cubic phases and identified the existence of co-existing phases.Non-equilibrium behaviours that influence MO phase properties and viscosities were found to change within the injector stream.
Rheology	[30,31,30,36,3737,57] This study	Rheological plate geometry experiment, study of flow behaviour of monoolein Using Rheology plate geometry and temperature sweeps Rheology plate geometry experiment combined with fluorescence particle tracking.	Characterized the viscoelastic properties, flow curves, shear rates, and transient behaviour of monoolein and other liquid crystalline systems under different flow conditions. Shear-thinning behaviour of MO/water mixtures was modelled using the Cross equation and the Carreau relationship. Cubic phase yielding and thinning behaviour was described. Non-equilibrium behaviours that influence MO phase properties and viscosities changes within the injector stream indicative of co-existing phases
Electron Microscopy	[47,57,48]	Utilized electron microscopy to study the morphology of bicontinuous cubic lipid phases and the incorporation of membrane proteins.	Visualized the lipid morphology, including the interconnected network of lipid phases and the arrangement of water channels, in bicontinuous cubic lipid phases. Observed co-existing phases and phase transformations in static samples.Examined the localization and arrangement of membrane proteins within bicontinuous cubic lipid phases, providing insights into their structural organization.
Dynamic Light Scattering	[8,57]	Dynamic light scattering was used to investigate the self-assembly and aggregation behaviour of monoolein.	Measured the size distribution, aggregation kinetics, and stability of monoolein self-assembled structures including vesicles and liquid crystalline phases.Observed phase transitions and co-existing phases.
Modelling studies	[283539]	Maxwell equations used to simulate the effects of flow. Leslie-Ericksen equations used to simulate the effects of flow.Finite Element Modelling used to simulate the effects of injection on the flow alignment, and phase transition of lipidic cubic phases.	Calculated the viscoelastic properties, average storage modulus for cubic phase structures and defined slip planes. Described the mesoscopic theory for weak flows of liquid crystalline polymers. Provided new insight into the shear thinning properties during continuous flow through an injector system.
Optical Cross-Polarization Measurements & Rheology	This study	Performs the first in-situ polarisation study of flow alignment, and phase transition of lipidic cubic phases during continuous flow injection.Studied the rheological properties of monoolein under constant flow conditions.	Experimental confirmation of injection induced phase heterogeneity in monoolein. Spatially resolved rheological measurements provide new insights into the formation of the metastable lamellar phase, concentrated at the edges of the sample. Flow visualisation rheology detected partitioning within the sample stream close to the wall which varied as a function of flow rate. Important for determining sample injection characteristics. New observation of a concentrated highly viscous cubic phase in the inner part of the stream and a much less viscous lamella rich phase at the edges of the stream close to the walls.Injector in-situ optical birefringence data supports both current rheology data and previous predictions from finite element simulations.

rheology and polarisation results show that the cubic phase can recover once the external shear force is halted or decreased (Fig. 3 and Figure S2). Similarly, shear-thinning behaviour has been previously measured for the cubic, hexagonal, and lamellar phases, where the cubic phase has the highest viscosity [33,42,51,59]. The Cross equation, $\frac{\eta_0-\eta}{\eta-\eta_\infty} = (K\gamma)^m$, was applied to fit the shear-thinning behaviour of such complex systems, where K is the Cross constant, m is the power-law exponent, η is the shear viscosity, η_0 is zero-shear viscosity, and η_∞ is the infinite-shear viscosity. The estimated power-law exponent approached unity for the pseudo-plastic systems [51]. In previous modelling study by Berntsen et.al [44], a near unity exponent simulated the flow dependent shear viscosity for the MO/water mixture during injection, where a zero-wall velocity was assumed. If, however, slippage occurs, as indicated in our studies, a thin layer of the fluid will form at the walls leading to higher localized shear rates. The flow localization of the sheared layers [60 59] creates non-uniform deformation of the fluid sample. The flow instability with the wall slip boundary might result in the metastable lamellar structure detected in the optical birefringence data. This is consistent with our polarisation studies and previous SAXS data showing that co-existing phases, cubic and lamellar, are present in the lipid stream [44]. In other injector systems the existence of this phase is not always present in the sample stream [23].

Another important factor to be considered is the yielding properties of the sample. As predicted by the slip-plane model, the MO/water cubic phase system is clearly able to maintain stable flow after yielding but means that bulk rheology measurements are less trustworthy above the yield strain (Fig. 4b). This is also demonstrated in the optical injector data when the change from high to low flow rate resulted in the momentary existence of birefringence (lamellar) which then reverted to a more stabilised cubic phase upon relaxation. Such behaviour makes prediction of fluid flow difficult when using simulations that assume homogeneous flow as we are not certain of the location of the yielded regions in flow, or their consistency.

To further understand the complex behaviour of MO, we investigated MO flow characterization using fluorescence confocal microscopy. By tracking the velocity of particles in the MO sample, we were able to characterize the flow within the sample stream. The calculated and experimental profiles showed good agreement when the experimentally determined power-law exponents were used in the calculation (Fig. 6). The cubic phase is a shear-thinning yield stress fluid, and a high-level simulation of its flow predicts the regions of high shear rate and flow and low shear rate within the capillary. In terms of the structure of the matrix, it is anticipated that the high shear rate regions at the wall cause the breakdown of the cubic phase and result in a metastable lamellar phase forming, as the bicontinuous structure is disrupted. This perspective is consistent with the observed birefringence of the cubic phase in the injector data, where birefringent lamellar phase is observed within the sample stream as the cubic phase emerges from the needle. What the present studies and previous finite element modelling work [44] both suggest is that under continuous flow, either in a capillary or in an injector system, the stream undergoes extreme deformation of the phase (i.e. cubic to lamellar) while the internal portion of the stream remains predominantly undeformed (i.e. cubic) which agrees with the high shear/low shear regions identified in our flow characterisation studies (Fig. 6).

The data suggests that shear banding effects occur in the flowing material (Figs. 6 and 7). Shear-banding phenomena are well-known in polymeric and colloidal systems as well as other liquid crystalline materials and can make consistent measurements of flow and rheology challenging [62]. Here, we can only speculate on the impact such behaviour would have on the actual fluid structure but think it likely a change from homogeneous to heterogeneous flow could cause formation of a cubic phase inside a shell of lamellar phase, also supported by our birefringence data. Although we can only speculate at this point, this is also supported by the enhanced resolution of this transition in our confocal microscopy study.

Clear banding and slowing of the fluorescence particles close to the wall (Fig. 8) until the internal velocity of the stream pushes the particles forward, resulted in removal of the 'plug', which allows the particles to move freely again near the wall. This seems to be a repetitive cycle, which may explain why the existence of the lamellar phase is not consistently present within the sample stream and emerges in and out of the data. [23,44]. The faster the flow rate, the greater the heterogeneity detected in the sample. For the highest flow rate tested (1000 μl/h), the sample reached speeds of ~ 120 μm/s (1.2 nl/s) which is equivalent to the slowest injector velocity (Table S1). Therefore, it is extrapolated that at higher injector velocities (200 μm/s, 1.9 nl/s) this will result in more prominent partitioning and metastable phase existence and this holds true in the birefringence data for the 60 % MO sample. However, for the 410 μm/s (3.9 nl/s) experiment, very little birefringence is detected as this may result in a reduction in size of the metastable phase region that may not to be detected in our setup.

5. Conclusion

Building on previous observations of phase changes in the MO during HVI continuous flow[23,44], this study demonstrated that injecting the MO sample leads to sample phase heterogeneity. Specifically, it resulted in the formation of a concentrated highly viscous cubic phase in the inner part of the stream, while a less viscous lamellar-rich phase formed near the walls. The hypothesis proposed that the MO/water mixture, when subjected to continuous flow conditions during injections, would exhibit non-equilibrium behaviours that would influence its phase properties and self-assembly structures. The study introduced new concepts by observing the formation of a concentrated highly viscous cubic phase and a less viscous lamellar-rich phase in the sample stream, providing valuable insights into the system's behaviour under injection conditions which has not been investigated before.

The study's key improvements compared to findings in the literature [31–39] include the comprehensive characterization of the MO/water mixture's dynamic behaviour within an injection system used for sample delivery. By employing rheology, particle tracking flow measurements, and optical cross-polarization measurements, this study gained fresh physical insights into the phase behaviour and shear-thinning properties of the MO/water mixture during continuous flow experiments. These techniques collectively deepened our understanding of the system's dynamics and provided valuable information about its behaviour when using HVIs as a delivery system. The findings contribute to the optimization of HVI experiments and have implications beyond X-ray serial crystallography, particularly in the context of drug delivery and X-ray characterisation of other potential self-assembly materials.

Based on the findings, future research focus on providing a more *in-depth understanding of the mechanisms underlying the formation of the observed phases and their impact on crystal formation, stability, and applications in drug delivery. Moreover, exploring the dynamic behaviour of the MO/water mixture in contexts beyond X-ray crystallography opens up* many new and exciting possiblities for optimizing a range of applications, including targeted drug delivery. *Additionally, utilizing HVIs as a delivery tool to characterize other radiation-sensitive high-viscosity materials presents a promising avenue for future investigation.*

Declaration of Competing Interest

The authors declare that they have no known competing financial interests or personal relationships that could have appeared to influence the work reported in this paper.

Data availability

Data will be made available on request.

Acknowledgements

Confocal microscopy was performed using instruments situated in and maintained by the Katharina Gaus Light Microscopy Facility (KGLMF) at the Mark Wainwright Analytical Centre, UNSW, Sydney, Australia.

Funding.

This work was partial support from the Australian Research Council (ARC LE200100221).

Appendix A. Supplementary data

Supplementary data to this article can be found online at https://doi.org/10.1016/j.jcis.2023.09.093.

References

[1] C.V. Kulkarni, W. Wachter, G. Iglesias-Salto, S. Engelskirchen, S. Ahualli, Monoolein: a magic lipid? Phys. Chem. Chemical Phys. 13 (8) (2011) 3004–3021.
[2] C. Darmanin, S. Sarkar, L. Castelli, C.E. Conn, Effect of lipidic cubic phase structure on functionality of the dopamine 2L receptor: implications for in meso crystallization, Crystal Growth & Design 16 (9) (2016) 5014–5022.
[3] C.E. Conn, C. Darmanin, X. Mulet, S. Le Cann, N. Kirby, C.J. Drummond, High-throughput analysis of the structural evolution of the monoolein cubic phase in situ under crystallogenesis conditions, Soft Matter 8 (7) (2012) 2310–2321.
[4] L. van 't Hag, C. Darmanin, T.C. Le, S. Mudie, C.E. Conn, C.J. Drummond, In meso crystallization: Compatibility of different lipid bicontinuous cubic mesophases with the cubic crystallization screen in aqueous solution, Crystal Growth & Design 14 (4) (2014) 1771–1781.
[5] J.L. Miller-Gallacher, R. Nehme, T. Warne, P.C. Edwards, G.F.X. Schertler, A.G. W. Leslie, C.G. Tate, The 2.1 angstrom resolution structure of cyanopindolol-bound beta(1)-adrenoceptor identifies an intramembrane Na+ Ion that stabilises the ligand-free receptor, PLoS One1 9 (3) (2014).
[6] Y.Y. Kang, X.E. Zhou, X. Gao, Y.Z. He, W. Liu, A. Ishchenko, A. Barty, D. Sathish, O. Yefanov, G.W. Han, Q.P. Xu, P.W. de Waal, J.Y. Ke, M.H.E. Tan, C.H. Zhang, A. Moeller, G.M. West, B.D. Pascal, N. Van Eps, L.N. Caro, S.A. Vishnivetskiy, R. J. Lee, K.M. Suino-Powell, X. Gu, K. Pal, J.M. Ma, X.Y. Zhi, S. Boutet, G.J. Williams, M. Messerschmidt, C. Gati, N.A. Zatsepin, D.J. Wang, D. James, S. Basu, S. Roy-Chowdhury, C.E. Conrad, J. Coe, H.G. Liu, S. Lisova, C. Kupitz, I. Grotjohann,

R. Fromme, Y. Jiang, M.J. Tan, H.Y. Yang, J. Li, M.T. Wang, Z. Zheng, D.F. Li, N. Howe, Y.M. Zhao, J. Standfuss, K. Diederichs, Y.H. Dong, C.S. Potter, B. Carragher, M. Caffrey, H.L. Jiang, H.N. Chapman, J.C.H. Spence, P. Fromme, U. Weierstall, O.P. Ernst, V. Katritch, V.V. Gurevich, P.R. Griffin, W.L. Hubbell, R. C. Stevens, V. Cherezov, K. Melcher, H.E. Xu, Crystal structure of rhodopsin bound to arrestin by femtosecond X-ray laser, Nature 523 (7562) (2015), 561-7.

[7] M. Caffrey, A comprehensive review of the lipid cubic phase or in meso method for crystallizing membrane and soluble proteins and complexes, Acta Crystallogr F 71 (2015) 3–18.

[8] C.E. Conn, C. Darmanin, X. Mulet, M. Moghaddam, J. Varghese, C.J. Drummond, Enhanced uptake of integral membrane proteins by cubic nanoparticles, Biophysical Journal 98 (3) (2010) 88a–a.

[9] X. Mulet, D.F. Kennedy, C.E. Conn, A. Hawley, C.J. Drummond, High throughput preparation and characterisation of amphiphilic nanostructured nanoparticulate drug delivery vehicles, Int J Pharmaceut 395 (1–2) (2010) 290–297.

[10] R. Varghese, S. Salvi, P. Sood, B. Kulkarni, D. Kumar, Cubosomes in cancer drug delivery: A review, Colloid Interfac Sci 46 (2022).

[11] T.T. Nguyen, T.T.D. Nguyen, N.M.A. Tran, G.V. Vo, Lipid-based nanocarriers via nose-to-brain pathway for central nervous system disorders, Neurochemical Research 47 (3) (2022) 552–573.

[12] P. Nogly, V. Panneels, G. Nelson, C. Gati, T. Kimura, C. Milne, D. Milathianaki, M. Kubo, W. Wu, C. Conrad, J. Coe, R. Bean, Y. Zhao, P. Bath, R. Dods, R. Harimoorthy, K.R. Beyerlein, J. Rheinberger, D. James, D. DePonte, C. Li, L. Sala, G.J. Williams, M.S. Hunter, J.E. Koglin, P. Berntsen, E. Nango, S. Iwata, H. N. Chapman, P. Fromme, M. Frank, R. Abela, S. Boutet, A. Barty, T.A. White, U. Weierstall, J. Spence, R. Neutze, G. Schertler, J. Standfuss, Lipidic cubic phase injector is a viable crystal delivery system for time-resolved serial crystallography, Nat. Commun. 7 (2016).

[13] P. Nogly, D. James, D.J. Wang, T.A. White, N. Zatsepin, A. Shilova, G. Nelson, H. G. Liu, L. Johansson, M. Heymann, K. Jaeger, M. Metz, C. Wickstrand, W.T. Wu, P. Bath, P. Berntsen, D. Oberthuer, V. Panneels, V. Cherezov, H. Chapman, G. Schertler, R. Neutze, J. Spence, I. Moraes, M. Burghammer, J. Standfuss, U. Weierstall, Lipidic cubic phase serial millisecond crystallography using synchrotron radiation, IUCRJ 2 (2015) 168–176.

[14] U. Weierstall, D. James, C. Wang, T.A. White, D. Wang, W. Liu, J.C.H. Spence, R. B. Doak, G. Nelson, P. Fromme, R. Fromme, I. Grotjohann, C. Kupitz, N.A. Zatsepin, H. Liu, S. Basu, D. Wacker, G.W. Han, V. Katritch, S. Boutet, M. Messerschmidt, G. J. Williams, J.E. Koglin, M.M. Seibert, M. Klinker, C. Gati, R.L. Shoeman, A. Barty, H.N. Chapman, R.A. Kirian, K.R. Beyerlein, R.C. Stevens, D. Li, S.T.A. Shah, N. Howe, M. Caffrey, V. Cherezov, Lipidic cubic phase injector facilitates membrane protein serial femtosecond crystallography, Nat. Commun. 5 (2014).

[15] W. Liu, D. Wacker, C. Gati, G.W. Han, D. James, D.J. Wang, G. Nelson, U. Weierstall, V. Katritch, A. Barty, N.A. Zatsepin, D.F. Li, M. Messerschmidt, S. Boutet, G.J. Williams, J.E. Koglin, M.M. Seibert, C. Wang, S.T.A. Shah, S. Basu, R. Fromme, C. Kupitz, K.N. Rendek, I. Grotjohann, P. Fromme, R.A. Kirian, K. R. Beyerlein, T.A. White, H.N. Chapman, M. Caffrey, J.C.H. Spence, R.C. Stevens, V. Cherezov, Serial femtosecond crystallography of G protein-coupled receptors, Science 342 (6165) (2013) 1521–1524.

[16] L.C. Johansson, D. Arnlund, T.A. White, G. Katona, D.P. DePonte, U. Weierstall, R. B. Doak, R.L. Shoeman, L. Lomb, E. Malmerberg, J. Davidsson, K. Nass, M.N. Liang, J. Andreasson, A. Aquila, S. Bajt, M. Barthelmess, A. Barty, M.J. Bogan, C. Bostedt, J.D. Bozek, C. Caleman, R. Coffee, N. Coppola, T. Ekeberg, S.W. Epp, B. Erk, H. Fleckenstein, L. Foucar, H. Graafsma, L. Gumprecht, J. Hajdu, C.Y. Hampton, R. Hartmann, A. Hartmann, G. Hauser, H. Hirsemann, P. Holl, M.S. Hunter, S. Kassemeyer, N. Kimmel, R.A. Kirian, F.R.N.C. Maia, S. Marchesini, A.V. Martin, C. Reich, D. Rolles, B. Rudek, A. Rudenko, I. Schlichting, J. Schulz, M.M. Seibert, R. G. Sierra, H. Soltau, D. Starodub, F. Stellato, S. Stern, L. Struder, N. Timneanu, J. Ullrich, W.Y. Wahlgren, X.Y. Wang, G. Weidenspointner, C. Wunderer, P. Fromme, H.N. Chapman, J.C.H. Spence, R. Neutze, Lipidic phase membrane protein serial femtosecond crystallography, Nature Methods 9 (3) (2012) 263–265.

[17] P. Berntsen, R. Sharma, M. Kusel, B. Abbey, C. Darmanin, Lipidico injection protocol for serial crystallography measurements at the australian synchrotron, J. Vis. Exps 163 (2020).

[18] L. Zhu, U. Weierstall, V. Cherezov, W. Liu, Serial femtosecond crystallography of membrane proteins, Adv. Exp. Med. Biol. 922 (2016) 151–160.

[19] J.M. Martin-Garcia, C.E. Conrad, G. Nelson, N. Stander, N.A. Zatsepin, J. Zook, L. Zhu, J. Geiger, E. Chun, D. Kissick, M.C. Hilgart, C. Ogata, A. Ishchenko, N. Nagaratnam, S. Roy-Chowdhury, J. Coe, G. Subramanian, A. Schaffer, D. James, G. Ketwala, N. Venugopalan, S.L. Xu, S. Corcoran, D. Ferguson, U. Weierstall, J.C. H. Spence, V. Cherezov, P. Fromme, R.F. Fischetti, W. Liu, Serial millisecond crystallography of membrane and soluble protein microcrystals using synchrotron radiation, IUCRJ 4 (2017) 439–454.

[20] M.O. Wiedorn, D. Oberthür, R. Bean, et al., Megahertz serial crystallography. Nat Commun 9 (2018) 4025, https://doi.org/10.1038/s41467-018-06156-7.

[21] S. Holmes, H.J. Kirkwood, R. Bean, et al., Megahertz pulse trains enable multi-hit serial femtosecond crystallography experiments at X-ray free electron lasers, Nat Commun 13 (2022) 4708, https://doi.org/10.1038/s41467-022-32434-6.

[22] D.J. Sellis, H. Qiu, M. Caffrey, 'Equilibrium' phase behavior of the monoolein/water system, Biophys. J. 74 (2) (1998) A203–A.

[23] D.J. Wells, P. Berntsen, E. Balaur, C.M. Kewish, P. Adams, A. Aquila, J. Binns, S. Boutet, H. Broomhall, C. Caleman, A. Christofferson, C.E. Conn, C. Dahlqvist, L. Flueckiger, F.G. Roque, T.L. Greaves, M. Hejazian, M. Hunter, M.H. Jazi, H. O. Jonsson, S.K. Pathirannahalage, R.A. Kirian, A. Kozlov, R.P. Kurta, H. Marman, D. Mendez, A. Morgan, K. Nugent, D. Oberthuer, H. Quiney, J. Reinhardt, S. Saha, J.A. Sellberg, R. Sierra, M. Wiedorn, B. Abbey, A.V. Martin, C. Darmanin, Observations of phase changes in monoolein during high viscous injection, J. Synchro. Rad. 29 (2022) 602–614.

[24] C.E. Conn, C. Darmanin, X. Mulet, A. Hawley, C.J. Drummond, Effect of lipid architecture on cubic phase susceptibility to crystallisation screens, Soft Matter 8 (26) (2012) 6884–6896.

[25] R. Mezzenga, C. Meyer, C. Servais, A.I. Romoscanu, L. Sagalowicz, R.C. Hayward, Shear rheology of lyotropic liquid crystals: A case study, Langmuir 21 (8) (2005) 3322–3333.

[26] J. Briggs, H. Chung, M. Caffrey, The temperature-composition phase diagram and mesophase structure characterization of the monoolein/water system, J. phys., II 6 (5) (1996) 723–751.

[27] H. Qiu, M. Caffrey, The phase diagram of the monoolein/water system: metastability and equilibrium aspects, Biomaterials 21 (3) (2000) 223–234.

[28] A.V. Martin, A. Kozlov, P. Berntsen, F.G. Roque, L. Flueckiger, S. Saha, T. L. Greaves, C.E. Conn, A.M. Hawley, T.M. Ryan, B. Abbey, C. Darmanin, Fluctuation X-ray diffraction reveals three-dimensional nanostructure and disorder in self-assembled lipid phases, Commun. Mater 1 (1) (2020) 1–8.

[29] J.M. Seddon, A.M. Squires, C.E. Conn, O. Ces, A.J. Heron, X. Mulet, G.C. Shearman, R.H. Templer, Pressure-jump X-ray studies of liquid crystal transitions in lipids, Philos T R Soc A 364 (1847) (2006) 2635–2655.

[30] M. Pisani, S. Bernstorff, C. Ferrero, P. Mariani, Pressure induced cubic-to-cubic phase transition in monoolein hydrated system, J. Phys. Chem. B 105 (15) (2001) 3109–3119.

[31] J.L. Jones, T.C.B. Mcleish, Rheological response of surfactant cubic phases, Langmuir 11 (3) (1995) 785–792.

[32] S. Radiman, C. Toprakcioglu, T. Mcleish, Rheological study of ternary cubic phases, Langmuir 10 (1) (1994) 61–67.

[33] G. Montalvo, M. Valiente, E. Rodenas, Rheological properties of the L phase and the hexagonal, lamellar, and cubic liquid crystals of the CTAB/benzyl alcohol/water system, Langmuir 12 (21) (1996) 5202–5208.

[34] J.M. Franco, J. Munoz, C. Gallegos, Transient and steady flow of a lamellar liquid-crystalline surfactant water-system, Langmuir 11 (2) (1995) 669–673.

[35] J.E. Moros, F. Cordobes, C. Gallegos, J.M. Franco, Linear viscoelasticity of concentrated polyethylene glycol tert-octylphenyl ether solutions, J Disper Sci Technol 22 (5) (2001) 409–420.

[36] P. Pitzalis, M. Monduzzi, N. Krog, H. Larsson, H. Ljusberg-Wahren, T. Nylander, Characterization of the liquid-crystalline phases in the glycerol monooleate/diglycerol monooleate/water system, Langmuir 16 (15) (2000) 6358–6365.

[37] A. Kelarakis, V. Castelletto, C. Chaibundit, J. Fundin, V. Havredaki, I.W. Hamley, C. Booth, Rheology and structures of aqueous gels of triblock(oxyethylene/oxybutylene/oxyethylene) copolymers with lengthy oxyethylene blocks, Langmuir 17 (14) (2001) 4232–4239.

[38] L. Messe, L. Corvazier, R.N. Young, A.J. Ryan, Phase Behavior of a poly(ethylene oxide)-block-poly(isoprene) copolymer in aqueous solutions: From liquid to solid state, Langmuir 18 (7) (2002) 2564–2570.

[39] L. Halasz, Z. Nemeth, J.P.T. Horanyi, A. Bota, Structural and viscoelastic properties of lamellar systems formed from concentrated nonionic surfactant solutions, Prog Coll. Pol. Sci. S 117 (2002) 159–166.

[40] R.G. Larson, M. Doi, Mesoscopic domain theory for textured liquid-crystalline polymers, J. Rheol. 35 (4) (1991) 539–563.

[41] G. Fritz, N.J. Wagner, E.W. Kaler, Formation of multilamellar vesicles by oscillatory shear, Langmuir 19 (21) (2003) 8709–8714.

[42] S. Mistry, P.L. Fuhrmann, A. de Vries, R. Karshafian, D. Rousseau, Structure-rheology relationship in monoolein liquid crystals, J. Colloid Interf. Sci. 630 (2023) 878–887.

[43] E. Tozzi, W. Hartt, Non-Newtonian laminar flow in pipes using radius, stress, shear rate or velocity as the independent variable, Phys. Fluids 33 (10) (2021).

[44] P. Berntsen, C. Darmanin, E. Balaur, L. Flueckiger, A. Kozlov, F.G. Roque, P. Adams, J. Binns, D. Wells, M.H. Jazi, S. Saha, A. Hawley, T. Ryan, S. Mudie, N. Kirby, B. Abbey, A.V. Martin, Stability, flow alignment and a phase transition of the lipidic cubic phase during continuous flow injection, J. Colloid Interf. Sci. 611 (2022) 588–598.

[45] C.E. Conn, C. Darmanin, S.M. Sagnella, X. Mulet, T.L. Greaves, J.N. Varghese, C. J. Drummond, Incorporation of the dopamine D2L receptor and bacteriorhodopsin within bicontinuous cubic lipid phases. 1. Relevance to in meso crystallization of integral membrane proteins in monoolein systems, Soft Matter 6 (19) (2010) 4828–4837.

[46] A. Cheng, B. Hummel, H. Qiu, M. Caffrey, A simple mechanical mixer for small viscous lipid-containing samples, Chem. Phys. Lipids 95 (1) (1998) 11–21.

[47] P. Berntsen, M.H. Jazi, M. Kusel, A.V. Martin, T. Ericsson, M.J. Call, R. Trenker, F. G. Roque, C. Darmanin, B. Abbey, The serial millisecond crystallography instrument at the Australian Synchrotron incorporating the "Lipidico" injector, Rev. Sci. Instrum. 90 (8) (2019).

[48] P. Berntsen, R. Sharma, M. Kusel, B. Abbey, C. Darmanin, Lipidico injection protocol for serial crystallography measurements at the australian synchrotron, J. Vis. Exp. 163 (2020) e61650.

[49] C.A. Schneider, W.S. Rasband, K.W. Eliceiri, NIH Image to ImageJ: 25 years of image analysis, Nat. Methods 9 (7) (2012) 671–675.

[50] J.C. Crocker, D.G. Grier, Methods of digital video microscopy for colloidal studies, J Colloid Interf Sci 179 (1) (1996) 298–310.

[51] R. Angelico, M. Carboni, S. Lampis, J. Schmidt, Y. Talmon, M. Monduzzi, S. Murgia, Physicochemical and rheological properties of a novel monoolein-based vesicle gel, Soft Matter 9 (3) (2013) 921–928.

[52] E. Eiser, F. Molino, G. Forte, X. Pithon, Flow in micellar cubic crystals, Rheol. Acta 39 (3) (2000) 201–208.

[53] S. Ansari, M.A.I. Rashid, P.R. Waghmare, D.S. Nobes, Measurement of the flow behavior index of Newtonian and shear-thinning fluids via analysis of the flow velocity characteristics in a mini-channel, Sn. Appl. Sci. 2 (11) (2020).
[54] D. Porter, J.R. Savage, I. Cohen, P. Spicer, M. Caggioni, Temperature dependence of droplet breakup in 8CB and 5CB liquid crystals, Phys. Rev. E 85 (4) (2012).
[55] J.R. Savage, M. Caggioni, P.T. Spicer, I. Cohen, Partial universality: pinch-off dynamics in fluids with smectic liquid crystalline order, Soft Matter 6 (5) (2010) 892–895.
[56] A. Datta, V.S. Tanmay, G.X. Tan, G.W. Reynolds, S.N. Jamadagni, R.G. Larson, Characterizing the rheology, slip, and velocity profiles of lamellar gel networks, J. Rheol. 64 (4) (2020) 851–862.
[57] F.T.Y. Wang, R.G. Larson, Thixotropic constitutive modeling of shear banding by boundary-induced modulus gradient in lamellar gel networks, J. Rheol. 67 (1) (2023) 35–51.
[58] A. Ganem-Quintanar, D. Quintanar-Guerrero, P. Buri, Monoolein: A review of the pharmaceutical applications, Drug Dev. Ind. Pharm. 26 (8) (2000) 809–820.
[59] A. Akbari, P. Sheath, S.T. Martin, D.B. Shinde, M. Shaibani, P.C. Banerjee, R. Tkacz, D. Bhattacharyya, M. Majumder, Large-area graphene-based nanofiltration membranes by shear alignment of discotic nematic liquid crystals of graphene oxide, Nat. Commun. 7 (2016).
[60] J.B. Salmon, L. Becu, S. Manneville, A. Colin, Towards local rheology of emulsions under couette flow using dynamic light scattering, Eur. Phys. J. E. Soft Matter 10 (3) (2003) 209–221.
[61] N. Huang, G. Ovarlez, F. Bertrand, S. Rodts, P. Coussot, D. Bonn, Flow of wet granular materials, Phys. Rev. Letters 94 (2) (2005).
[62] T. Divoux, M.A. Fardin, S. Manneville, S. Lerouge, Shear banding of complex fluids, Annu. Rev. Fluid Mech. 48 (2016) 81–103.